Impact of cirrus crystal shape on solar spectral irradiance: A case study for subtropical cirrus

Manfred Wendisch,[1,2] Peter Pilewskie,[2,3] John Pommier,[4] Steve Howard,[4] Ping Yang,[5] Andrew J. Heymsfield,[6] Carl G. Schmitt,[6] Darrel Baumgardner,[7] and Bernhard Mayer[8]

Received 28 July 2004; revised 12 November 2004; accepted 7 December 2004; published 4 February 2005.

[1] Profiles of in situ measurements of ice crystal size distribution of subtropical cirrus were used to calculate solar spectral irradiances above and below the clouds. Spheres and nonspherical ice crystal habits (columns, hollows, plates, bullets, and aggregates) were assumed in the calculations. The simulation results were compared to irradiance measurements from the NASA Solar Spectral Flux Radiometer. The microphysical and radiation data were collected by three aircraft during CRYSTAL-FACE. Two cirrus cases (optical thickness of about 1 and 7) from two mission dates (26 and 23 July 2002) were investigated in detail. The measured downwelling and upwelling irradiance spectra above the cirrus could mostly be reproduced by the radiation model to within ±5–10% for most ice crystal habits. Below the cirrus the simulations disagreed with the measured irradiances due to surface albedo variability along the flight track, and nonoptimal colocation between the microphysical and irradiance measurements. The impact of shape characteristics of the crystals was important for the reflected irradiances above the optically thin cirrus, especially for small solar zenith angles, because in this case single-scattering dominated the solar radiation field. For the cirrus of moderate optical thickness the enhanced multiple scattering tended to diminish particular shape features caused by nonspherical single-scattering. Within the ice absorption bands the shape-related differences in the absorption characteristics of the individual nonspherical ice crystals were amplified if multiple scattering prevailed. Furthermore, it was found that below the cloud the shape sensitivity of the downwelling irradiance spectra is larger compared to the nonsphericity effects on reflected irradiances above the cirrus. Finally, it was shown that the calculated cirrus solar radiative forcing could vary by as much as 26% depending on the ice crystal habit.

Citation: Wendisch, M., P. Pilewskie, J. Pommier, S. Howard, P. Yang, A. J. Heymsfield, C. G. Schmitt, D. Baumgardner, and B. Mayer (2005), Impact of cirrus crystal shape on solar spectral irradiance: A case study for subtropical cirrus, *J. Geophys. Res.*, *110*, D03202, doi:10.1029/2004JD005294.

1. Introduction

[2] Cirrus clouds play an important role in weather processes and the Earth's climate [*Liou*, 1986; *Ramaswamy and Ramanathan*, 1989; *Sherwood*, 1999; *Lynch et al.*, 2002], because they significantly modify the solar and infrared radiation within the atmosphere. This modification is realized by scattering and absorption of solar radiation and by absorption and emission of infrared radiation. The scattering reduces the solar radiation reaching the Earth's surface and thus results in a surface cooling effect. On the other hand, cirrus clouds absorb upwelling infrared radiation emitted by the surface and lower atmosphere and emit at much lower temperatures than the surface, effectively reducing the infrared energy escaping the Earth-atmosphere system. The net effect of cirrus on surface temperature depends on several factors including cloud height, cloud geometrical thickness, and cirrus microphysical properties (ice crystal size and shape). Perhaps the least known of these factors, ice crystal shape, makes it very complicated to quantify the impact of cirrus clouds on global climate.

[1]Leibniz-Institute for Tropospheric Research (IfT), Leipzig, Germany.
[2]Earth Science Division, National Aeronautics and Space Administration (NASA), Ames Research Center (ARC), Moffett Field, California, USA.
[3]Now at Laboratory for Atmospheric and Space Physics (LASP), Program in Atmospheric and Oceanic Science, University of Colorado, Boulder, Colorado, USA.
[4]Bay Area Environmental Research (BAER) Institute, Sonoma, California, USA.
[5]Department of Atmospheric Sciences, Texas A&M University, College Station, Texas, USA.
[6]Mesoscale and Microscale Meteorology Division, National Center for Atmospheric Research (NCAR), Boulder, Colorado, USA.
[7]Center for Atmospheric Research, University of Mexico (UNAM), Mexico City, Mexico.
[8]Institute for Physics of the Atmosphere, German Aerospace Center (DLR), Oberpfaffenhofen, Germany.

0148-0227/05/2004JD005294$09.00

[3] There are also climate feedback processes related to cirrus clouds. For example, anthropogenic greenhouse gases can increase the surface temperature, which might result in an increased frequency and intensity of deep convective systems, which may affect cirrus cloudiness. Hence the net effect of increased greenhouse gas concentrations on surface temperature also depends on the response of cirrus to the changing environment. Cirrus cloud properties may change due to natural and anthropogenic aerosols. Elevated aerosol particles may affect ice nucleation and thus change the numbers and sizes of cirrus ice crystals. These cirrus cloud modifications would ultimately affect radiation budgets and climate.

[4] The microphysical characteristics of cirrus clouds are closely linked to their optical properties. Several, mostly theoretical, studies have been published on this subject [e.g., *Kinne and Liou*, 1989; *Mishchenko et al.*, 1996; *Tsay et al.*, 1996; *Macke et al.*, 1998; *Zhang et al.*, 1999; *Yang et al.*, 2000]. Only sparse experimental data are presented in literature [e.g., *Francis et al.*, 1999], which, however, are limited to broadband (solar and infrared) cirrus optical properties.

[5] In this paper we concentrate on solar radiative effects of cirrus ice crystals. We include airborne microphysical in situ measurements (crystal number size distribution) into radiative transfer calculations in order to quantify (1) the impact of crystal habit on solar spectral irradiances above and below the clouds, and (2) the cirrus radiative forcing as a function of ice crystal habit. The primary goal of this paper is to evaluate the spectral radiative effects due to the usually nonspherical shape of ice crystals in cirrus clouds using actual microphysical data. The conclusions are supported by comparing the simulations with solar spectral irradiance measurements, which are colocated as best as practically possible with the microphysical sampling. In this way the measurement-based calculations are constrained by the solar spectral irradiance data collected above and below the cirrus clouds.

[6] In section 2 the experimental instrumentation and modeling tools used in this paper are introduced. Subsection 2.1 describes the field experiment from which the data in this study were obtained, as well as the microphysical and radiation instrumentation. Subsection 2.2 introduces the modeling tools applied to simulate the scattering/absorption of solar radiation by individual ice crystals, crystal populations, and to calculate the solar atmospheric radiative transfer including multiple scattering. In section 3 the influence of crystal habits on the spectral optical properties of individual ice crystals (subsection 3.1) and crystal populations (subsection 3.2) is investigated. In the major part of this paper the nonsphericity effects on the spectral irradiance above and below the cirrus clouds (subsection 3.3), and on the cirrus radiative forcing (subsection 3.4) are quantified. Section 4 provides a summary and conclusions.

2. Methods and Materials

2.1. Experiment

2.1.1. CRYSTAL-FACE

[7] In this paper, microphysical and radiation measurements from the Cirrus Regional Study of Tropical Anvils and Cirrus Layers - Florida Area Cirrus Experiment (CRYSTAL-FACE) are analyzed [*Jensen et al.*, 2004]. CRYSTAL-FACE was conducted to study the microphysical, dynamical, and radiative properties of tropical and subtropical cirrus anvil and layer clouds. The data were collected around Florida and the Caribbean Sea in July 2002 from six aircraft and several surface sites. Measurements from the NASA ER-2 and WB-57F, as well as the Naval Research Lab CIRPAS (Center for Interdisciplinary Remotely-Piloted Aircraft Studies) Twin-Otter (type UV-18A) will be the focus of this study. The WB-57F carried a suite of microphysical instruments (see subsection 2.1.2.1) to probe the cloud characteristics. The ER-2 and the Twin-Otter were both equipped with identical versions of solar spectral irradiance sensors (see subsection 2.1.2.2) to measure downwelling and upwelling irradiance spectra above (ER-2) and below (Twin-Otter) the cirrus clouds. Two specific cirrus cases have been investigated in detail (subsection 2.1.3).

2.1.2. Instrumentation

2.1.2.1. Microphysical Measurements

[8] Two different approaches to measure the ice crystal size distribution were applied: (1) The Video Ice Particle Sampler (VIPS; size range 0–300 μm with an equidistant resolution of 10 μm) directly collects the ice particles on a rotating, oil-covered replicator [*Heymsfield and McFarquhar*, 1996]. The collected crystals are observed with a digital video camera. The crystal size distribution is retrieved from the images with an objective algorithm after the flights. (2) Three optical size spectrometers covering overlapping size ranges are combined to obtain the composite crystal size distribution. These three instruments are the Cloud Aerosol Precipitation Spectrometer (CAPS), the Signal Processing Package (SPP), and the Cloud Particle Imager (CPI).

[9] The CAPS is a combination of the Cloud Aerosol Spectrometer (CAS; size range 0.5–44 μm) and the Cloud Imaging Probe (CIP; size range 50–1600 μm) and is introduced by *Baumgardner et al.* [2002]. The SPP (model 100, SPP-100; size range 2–47 μm) is a modified Forward Scattering Spectrometer Probe (FSSP-100), manufactured by Particle Measuring Technology, and is equipped with an electronics signal processing package from Droplet Measurement Technology. The revised signal electronics eliminates deadtime losses and improves the size resolution. The CPI (manufactured by SPEC Inc.) captures complete crystal images with a high size resolution (3 μm). However, the field of view and sampling threshold limit the size range to approximately 15–300 μm. The size distributions from the three instruments (CAPS/SPP/CPI) were combined by averaging the concentrations from the probes in overlapping regions. Additional corrections were made to the SPP for sample volume dependencies on particle size.

[10] The measurement uncertainties for the CAPS have been documented by *Baumgardner et al.* [2002], but these are for spherical water particles. Instead of adding to the uncertainty in case of nonspherical ice crystals, the averaging of the size distributions in overlapping size ranges is expected to decrease the uncertainties since there are differences in both the sample volumes of the SPP-100 and the CAS and certainly between these two instruments and the CPI. The uncertainty in the sizing with the CAS, due to

aspherical particles is estimated to 30%. The projected-area uncertainty for optical calculations is about 40%, but it could be as high as 50% if the particles are columns. However, if the majority of the sub-50 μm crystals are roughly symetrical in shape, the uncertainty in the size measurements is probably no more than 30% and similarly the projected area uncertainty will be 40%.

[11] For the specific measurement case discussed below, the VIPS worked extremely well. The sampling volume of the particles imaged by the VIPS is generally well known. All of the VIPS particles are essentially in focus, because they land on a substrate and thus there are no serious depth of field problems as with the imaging probes. The particle sizes are sufficiently large such that collection efficiency is essentially unity. Therefore the concentration measurements of the VIPS are quite accurate. No particle breakup on the VIPS substrate occurred because the particles were not too large in the case investigated here. There is some sizing uncertainty due to the exact focus of the VIPS. This could have led to a 10–20% overestimate in the particle size of the VIPS measurements.

[12] From the number size distributions $\frac{dN}{d\log D}$ (N being the number concentration in each size bin in dm^{-3}; and D representing the maximum particle dimension in μm) measured by the VIPS or the combination of CAPS/SPP/CPI, the total number concentration (N_T in dm^{-3}) of the ice crystal population was calculated by integration. Also the ice water content (IWC in mg m^{-3}) was derived from the size distribution measurements. The ice water path (IWP in g m^{-2}) was estimated by vertical integration of the profile data of IWC. The size distribution instruments also provided the total geometrical cross section of the ice crystals. This has been used to estimate the volume extinction coefficient in the visible spectral range $b_{ext,vis}$ (in km^{-1}). It was approximated by the geometrical optics limiting value of twice the total geometrical cross section of the crystals. By vertical integration of profile data of $b_{ext,vis}$ the visible optical thickness (τ_{vis}, dimensionless) was obtained. Finally the effective radius (r_{eff} in μm) of the cirrus cloud was estimated using the approximation $r_{eff} \simeq \frac{3}{2} \cdot \frac{IWP}{\tau_{vis}}$ [*Slingo*, 1990].

[13] From the microphysical measurements by the WB-57F only profile (vertically dispersed) data were used in this study. Profile measurements actually cover some horizontal extent which has to be kept in mind when interpreting the profile data from the WB-57F shown below.

2.1.2.2. Solar Spectral Irradiance Measurements

[14] The radiation measurements were performed using the NASA Solar Spectral Flux Radiometer (SSFR). The instrument and its calibration is described in detail by *Pilewskie et al.* [2003]. The SSFR measures downwelling and upwelling irradiance spectra between 350–1670 nm (Full Width at Half Maximum, FWHM ≈ 9–12 nm). The radiation is collected by two hemispheric, upward and downward looking optical inlets (with a cosine angular response) and transferred, via fiber optics, to four separate multichannel spectroradiometers (manufactured by Zeiss GmbH). One pair of spectroradiometers is used to measure the downwelling, another pair observes the upwelling irradiance spectra. One type of spectroradiometers covers the ultraviolet (UV), visible (VIS), and near-infrared (NIR) wavelength range from 350 nm to 1000 nm. The second set of spectroradiomters is applied to detect the extended NIR wavelength range from 900 nm to 1670 nm. The measurements by the two spectroradiometers for each hemisphere are combined to yield a composite spectrum over the entire UV-VIS-NIR spectral range. However, due to decreased sensitivity of the spectroradiometers near the limit of their respective wavelength ranges, parts of the overlapping regions between the spectroradiometers (930–983 nm) have been excluded from the analysis.

[15] Two identical versions of the SSFR have been installed on the ER-2 and Twin-Otter airplanes. Both instruments have been calibrated in absolute irradiance units (W m^{-2} nm^{-1}) using a calibrated 1000 W tungsten halogen lamp before and after the campaign in the laboratory. In order to track calibration shifts during the experiment, laboratory and postflight secondary calibrations were done using 200 W lamp irradiance standards. The family of those calibrations were within 1% from 400–1650 nm wavelength. The wavelength calibration of the spectroradiometers has been confirmed using a variety of spectral line radiation sources. The overall estimated uncertainty for the SSFR spectral irradiance measurements is ±4% (for wavelengths λ = 400–770 nm) to ±6% ($\lambda \leq$ 400 nm and $\lambda \geq$ 770 nm). The downwelling irradiances from the ER-2 were filtered to remove those data collected when the cosine of solar zenith angle, $\cos(\theta_s)$, with respect to the aircraft differed by more than 1% from $\cos(\theta_s)$ with respect to the Earth-fixed coordinate system.

2.1.3. Investigated Cases

[16] The three criteria for the selection of the cases to be investigated were (1) available profile measurements of the microphysical properties through the cirrus clouds by the WB-57F, (2) available irradiance data above the cloud by the ER-2, and if possible, by the Twin-Otter below cloud, and (3) close colocation (in space and time) between the radiation aircraft (ER-2 and Twin Otter) and the microphysical measurements by the WB-57F. These criteria are extremely challenging; however, they are crucial for the data interpretation. After carefully screening the entire data set, only four cases fulfilled the three conditions: 7, 9, 23, and 26 July 2002. From these, two are discussed in detail in the text below (26 and 23 July 2002).

2.1.3.1. Optically Thin Cirrus: 26 July 2002

[17] The first cirrus cloud case analyzed here was observed on 26 July 2002. Figure 1 depicts that part of the flight tracks of the ER-2 and the WB-57F, where both aircraft were in close proximity on this day. The WB-57F penetrated a cirrus cloud in a descending profile pattern between 16 km and 13 km altitude. The ER-2 was flying above the cloud concurrently during the profile sampling by the WB-57F and maintained a nearly constant flight altitude at 19.9 km. The entire flight tracks of both aircraft were over the ocean.

[18] The number size distribution measurements collected by the VIPS during the descent of the WB-57F through the cirrus layer are not shown here. The curves peak at a maximum dimension of about 25 μm in a single mode. Because the radiative effects of the ice crystals are related to the cross section of the crystals, rather than to their number concentration, $\frac{dN}{d\log D}$ was converted into cross section size distributions by multiplying with the crystal cross section

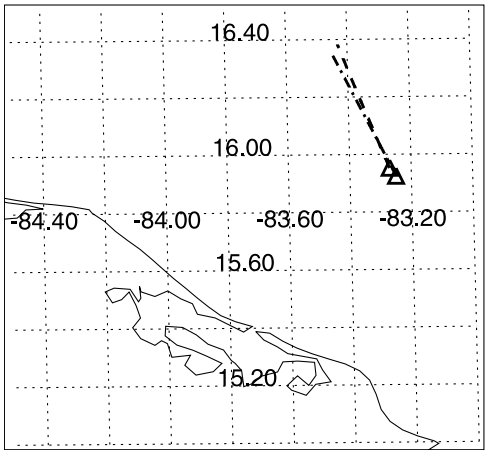

Figure 1. Map of the flight area for the measurements on 26 July. A 1.5° × 1.5° (corresponds to ≈167 km × 161 km) geographical grid is covered, and the numbers give the respective longitude and latitude. The coastline of parts of northern Honduras is included as a thin solid line. The flight paths of the ER-2 (thick dash-dotted line), and WB-57F (thick dashed line) are plotted for the time period between 1859:29 and 1904:08 UTC. The starting locations of the colocated flight paths are indicated as open triangles.

(assuming spherical crystal shape). The resulting distributions showed that in this case, ice crystals with a maximum dimension larger than 30 μm dominated the optical extinction. The VIPS measurement size range is biased toward the larger crystals. Therefore not all of the optically efficient larger particles were sampled by the VIPS.

[19] Figure 2 gives an overview of the vertical structure of the cirrus cloud observed on 26 July. In Figure 2a the profile of N_T is presented, and in Figure 2b the profile of the *IWC* is shown. This cirrus cloud extended from about 13.1 km to 15.4 km altitude. N_T ranged approximately between 100 and 300 dm^{-3}, the *IWC* mostly stayed below 8 mg m^{-3} within the entire cloud layer. The *IWP* was in the range of 7.5 g m^{-2}. A value of τ_{vis} of about 1 was derived, which is typical for an optically thin cirrus cloud. r_{eff} of this cirrus was estimated to be approximately 11 μm. The general macroscopic, microphysical, and optical characteristics of this cirrus cloud are summarized in Table 1.

2.1.3.2. Cirrus of Moderate Optical Thickness: 23 July 2002

[20] The second cirrus case investigated here was observed on 23 July 2002, when coordinated flights of three aircraft (ER-2, WB-57F, and Twin-Otter) were conducted. In Figure 3 the parts of the flight paths of the three aircraft analyzed here are shown. For practical reasons coordinating three aircraft (with different speeds) in the same geographical area and with one of the aircraft flying in clouds is quite complicated. Flight safety rules make it virtually impossible to have the three aircraft in the area at the same time. Therefore, first the two radiation aircraft (ER-2 and Twin-Otter) were simultaneously sampling the radiation field above and below the cloud, and 29 min after the radiation aircraft left the area the WB-57F profiled through the cloud to collect the microphysical data. The ER-2 was flying at a constant altitude of 20.7 km and the Twin-Otter at 3.6 km. The WB-57F penetrated into the cloud at 13 km and descended to about 6 km altitude. The flight paths of the ER-2 and the Twin-Otter in Figure 3 cover exactly the same time period. Because the Twin-Otter is much slower than the ER-2, the length of the flight leg of the Twin-Otter is shorter compared to that of the ER-2. Because of the 29-min time lag, the microphysical sampling of the WB-57F was not perfectly concurrent with the ER-2 and Twin-Otter radiative sampling, and this had to be considered in the data interpretation.

[21] The size distribution measurements for this case (not shown here) are a composite from the CAPS/SPP/CPI instruments and cover a larger size range than the VIPS. A local maximum in the number size distribution was observed around $D \approx 25$ μm, similar to the 26 July case. However, both the level and the variability in the measured $\frac{dN}{d\log D}$ were larger. A high number of small particles with less than 4 μm maximum dimension was detected. This had no serious impact on the solar radiation, which has been tested by sensitivity calculations in

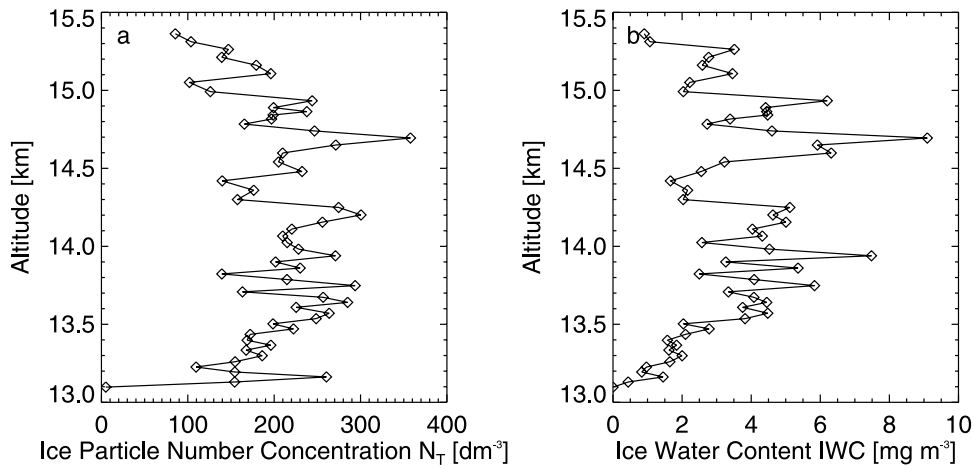

Figure 2. VIPS measurements (on board WB-57F aircraft) of the (left) ice particle number concentration N_T and (right) ice water content *IWC* for the measurements on 26 July.

Table 1. Summary of the General Characteristics of the Two Cirrus Cloud Cases From CRYSTAL-FACE Investigated in This Study

	26 July 2002 Optically Thin Cirrus (VIPS Data)	23 July 2002 Cirrus of Moderate Optical Thickness (CAPS/SPP/CPI Measurements)
Macroscopic		
Cloud base height, km	13.1	6.4
Cloud top height, km	15.4	8.0
Microphysical		
Maximum total number concentration N_T, dm^{-3}	300	15,000
Maximum Ice Water Content *IWC*, mg m^{-3}	8	550
Ice Water Path *IWP*, g m^{-2}, $IWP = \int IWC(z') \cdot dz'$	7.5	504
Optical		
Maximum volume extinction coefficient $b_{ext,vis}$, km^{-1}	0.8	8
Visible optical thickness $\tau_{vis} = \int b_{ext,vis}(z') \cdot dz'$	1	7
Effective radius r_{eff}, μm, $r_{eff} \simeq \frac{3}{2} \cdot \frac{IWP}{\tau_{vis}}$	11	108

which the small particles were removed from the size distribution. Because of the larger size range covered by the CAPS/SPP/CPI measurements, more optically efficient ice crystals were sampled compared to the VIPS.

[22] Profiles of N_T and *IWC* are presented in Figure 4. The major parts of the cirrus cloud extended from about 6.4 km to 8 km altitude. Above this layer some cirrus patches were sampled which were not representative for the entire flight path of the ER-2 and Twin-Otter. This has been shown by nadir Lidar observations from the ER-2 (M. McGill, private communication). Therefore, in the following radiative transfer calculations, only the major cloud layer between 6.4 to 8 km altitude has been considered. Including the cirrus patches above the primary cloud layer changed the simulated reflected and transmitted irradiance spectra at the flight levels by less than 5%.

[23] The general characteristics of the cirrus cloud observed on 23 July are compared with those of 26 July in Table 1. N_T was much higher on 23 July with maximum values of up to 15,000 dm^{-3}. The maximum *IWC* and the *IWP* was roughly seventy times higher compared to the 26 July case. τ_{vis} was approximately 7 for the 23 July case, which we categorize as moderate optical thickness. r_{eff} of this moderately thick cirrus is estimated to be approximately 108 μm.

2.2. Modeling

[24] For the simulation and interpretation of the SSFR observations above and below the cirrus clouds we used the following strategy: (1) First, the spectral single-scattering optical properties of the individual ice crystals were calculated as a function of the maximum particle dimension D and the wavelength λ (subsection 2.2.1). In order to quantify the impact of different crystal habits on solar radiation, these calculations assumed several crystal shapes: spheres, columns, hollows, plates, bullets, and aggregates. (2) Second, the single-scattering optical properties were combined with the observed profiles of ice crystal number size distributions to calculate the vertical distribution of the spectral volumetric optical properties of the ice crystal populations for the different crystal shapes (see subsection 2.2.2). (3) Third, the volumetric optical properties were used as input to a radiative transfer model to simulate the solar spectral irradiance above and below the cirrus in the flight levels of the ER-2 and Twin-Otter aircraft assuming different crystal habits (subsection 2.2.3).

2.2.1. Individual Ice Crystals

[25] The single-scattering optical properties of individual ice crystals (extinction cross section $C_{ext,\lambda}$, single-scattering albedo ω_λ, phase function p_λ, and asymmetry parameter g_λ) were computed for the different ice crystal habits. $C_{ext,\lambda}(D)$ quantifies the extinction of solar radiation by a particle with maximum dimension D. $\omega_\lambda(D)$ is defined as the ratio of scattering cross section to extinction cross section. $p_\lambda(\theta,D)$ describes the distribution of the

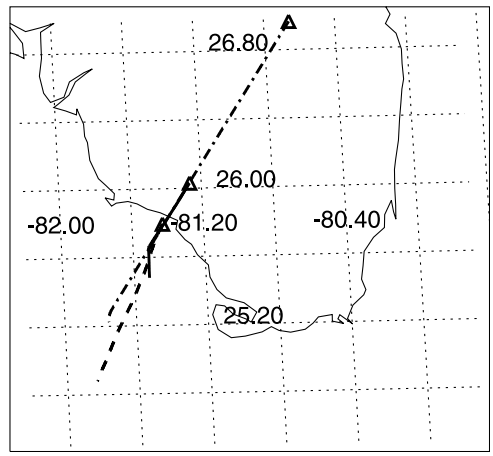

Figure 3. Same as Figure 1, but for 23 July. A 2.5° × 2.5° (corresponds to ≈278 km × 252 km) geographical grid is covered. The coastline of southern Florida is included as a thin solid line. Additionally to the flight paths of the ER-2 (thick dash-dotted line), and WB-57F (thick dashed line), the flight path of the Twin-Otter is plotted as a thick solid line. The two flight paths of the ER-2 and Twin-Otter were both flown between 2303:00 and 2320:00 UTC. The microphysical sampling with the WB-57F was performed 29 min after the two radiation aircraft had left the area (2349:04–2401:44 UTC). The starting locations of the flight paths of the three aircraft are indicated as open triangles.

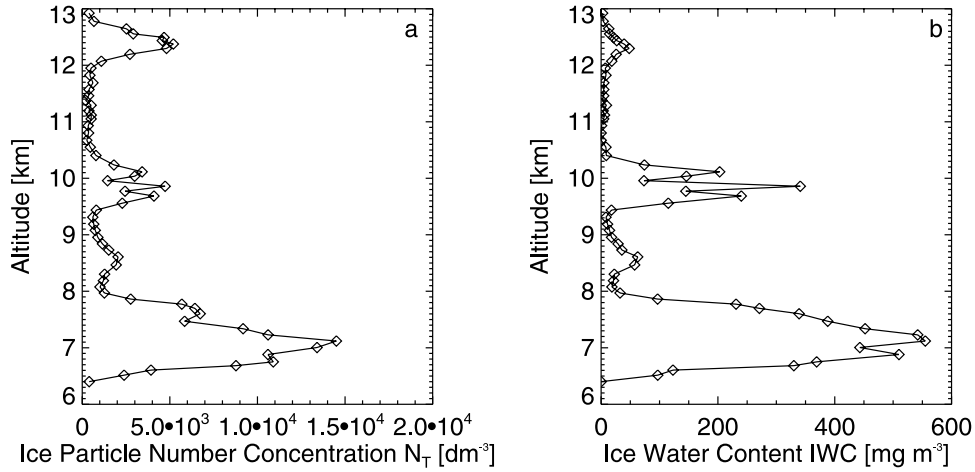

Figure 4. Same as Figure 2, but for 23 July. Size distribution measurements of the CAPS/SPP/CPI instruments on board the WB-57F aircraft were used for the integration.

scattered radiation as a function of the scattering angle θ. The first moment of the phase function, the so-called asymmetry parameter $g_\lambda(D)$, ranges between -1 and 1 and quantifies the asymmetry of the scattering pattern. g_λ values approaching 1 or -1 represent a highly asymmetric phase function, while values of g_λ around 0 characterize a symmetric phase function.

[26] The calculations were performed using an Improved Geometric Optics Method (IGOM) developed by *Yang and Liou* [1996]. In IGOM, the principles of geometric optics are employed to compute the near-field, which is mapped to the far-field on the basis of a rigorous electromagnetic relationship. The conventional ray-tracing technique gives a constant extinction efficiency (defined as the ratio of $C_{ext,\lambda}$ and the geometrical cross section of the particle) of 2 regardless of particle size. This nonrealistic result is circumvented in IGOM by accounting for the phase interferences between the rays. It should be pointed out that the tunneling effect [*Baran et al.*, 2001; *Mitchell*, 2002], which can be significant in the infrared and NIR wavelength regions [e.g., *Yang et al.*, 2003], is not considered in IGOM. However, this issue is not substantial in the spectral range covered by SSFR and thus the IGOM is reasonably accurate for our application [cf. *Liou et al.*, 2000]. The refractive indices used in the simulations were taken from Warren's compilation [*Warren*, 1984] with a modification based on the measurements by *Gosse et al.* [1995].

[27] The results of the calculations have been archived in an electronic library. 140 equidistant wavelengths from 300 to 1700 nm (10 nm steps) were used to cover the complete wavelength range of the SSFR. The ice crystal size spectrum was subdivided into 40 bins between 1 μm to 1500 μm.

2.2.2. Ice Crystals Populations

[28] The volumetric optical properties of the ice crystal populations were obtained by integration of the single-scattering optical properties ($C_{ext,\lambda}$, ω_λ, g_λ, and p_λ) weighted by the number size distribution $\frac{dN}{d\log D}$. This procedure corresponded to a number size distribution weighted averaging of the single-scattering optical properties.

[29] The spectral volume extinction coefficient $\langle b_{ext,\lambda}\rangle$ in units of km^{-1} was calculated by

$$\langle b_{ext,\lambda}\rangle = \int C_{ext,\lambda}(D') \cdot \frac{dN}{d\log D}(D') \cdot d\log D'. \quad (1)$$

In a similar manner the volumetric single-scattering albedo $\langle\omega_\lambda\rangle$ and the volumetric asymmetry parameter $\langle g_\lambda\rangle$ (both dimensionless) were obtained by

$$\langle\omega_\lambda\rangle = \frac{\int \omega_\lambda(D') \cdot C_{ext,\lambda}(D') \cdot \frac{dN}{d\log D}(D') \cdot d\log D'}{\langle b_{ext,\lambda}\rangle}, \quad (2)$$

$$\langle g_\lambda\rangle = \frac{\int g_\lambda(D') \cdot C_{sca,\lambda}(D') \cdot \frac{dN}{d\log D}(D') \cdot d\log D'}{\int C_{sca,\lambda}(D') \cdot \frac{dN}{d\log D}(D') \cdot d\log D'}, \quad (3)$$

with $C_{sca,\lambda} = \omega_\lambda \cdot C_{ext,\lambda}$. Additionally the volumetric phase function $\langle p_\lambda\rangle$ (unit of sr^{-1}) has been calculated by a similar weighting procedure:

$$\langle p_\lambda(\theta)\rangle = \frac{\int p_\lambda(\theta, D') \cdot C_{sca,\lambda}(D') \cdot \frac{dN}{d\log D}(D') \cdot d\log D'}{\int C_{sca,\lambda}(D') \cdot \frac{dN}{d\log D}(D') \cdot d\log D'}. \quad (4)$$

2.2.3. Calculation of Solar Spectral Irradiances

2.2.3.1. Model Features and Input

[30] The libRadtran (library for Radiative transfer) code by *Mayer and Kylling* [2005] was used in this study. libRadtran is a flexible and user-friendly model package which allows quick, yet accurate simulation of solar spectral irradiances. The discrete ordinate solver DISORT version 2.0 by *Stamnes et al.* [1988] with six streams was applied. For the meteorological input (static air temperature, relative humidity, and static air pressure) the tropical profile by *Anderson et al.* [1986] was merged with actual data from nearby drop sonde measurements (launched from the ER-2). For the aerosol microphysical properties the spring-summer rural aerosol profile by *Shettle* [1989]

was used in the boundary layer, assuming a visibility of 50 km. For altitudes above 2 km the background aerosol type by *Shettle* [1989] was chosen. For the radiative transfer calculations particular surface albedo measurements for the CRYSTAL-FACE area were used [*Wendisch et al.*, 2004].

[31] The cirrus microphysical model input consisted of the profiles of the volume extinction coefficient $\langle b_{ext,\lambda}\rangle$, the volumetric single-scattering albedo $\langle\omega_\lambda\rangle$, and the volumetric asymmetry parameter $\langle g_\lambda\rangle$ (or the volumetric phase function $\langle p_\lambda\rangle$). These volumetric cirrus optical properties were calculated on the basis of the single-scattering optical properties of the individual ice crystal ($C_{ext,\lambda}$, ω_λ, and g_λ, or p_λ) weighted with the profiles of the measured number size distribution (equations (1)–(4)). The calculated profiles of the volumetric cirrus optical properties have been interpolated onto the vertical model grid, which has a vertical resolution of 0.1 km (26 July case) or 0.02 km (23 July cirrus cloud), respectively.

2.2.3.2. Henyey-Greenstein Versus Exact Volumetric Phase Function

[32] The treatment of exact volumetric scattering phase functions in radiative transfer codes is often quite complex. Due to the sharp forward peak typical for ice particle populations, the often-used Legendre-expansion of $\langle p_\lambda\rangle$ requires thousands of terms for an adequate representation of all features, which is computationally time consuming. To circumvent this problem, the Henyey-Greenstein (HG) volumetric phase function ($\langle p_{HG,\lambda}\rangle$) is often applied as an approximation for the exact volumetric phase function:

$$\langle p_{HG,\lambda}\rangle = \frac{1-\langle g_\lambda\rangle^2}{\left(1+\langle g_\lambda\rangle^2 - 2\langle g_\lambda\rangle\cdot\cos\theta\right)^{\frac{3}{2}}}. \quad (5)$$

In this HG approximation only the volumetric asymmetry parameter $\langle g_\lambda\rangle$ is required and the computer time-consuming Legendre-expansion of the exact volumetric phase function is not needed. Instead the Legendre-coefficients for $\langle p_{HG,\lambda}\rangle$ are analytically given. The first Legendre-coefficient of $\langle p_{HG,\lambda}\rangle$ is 1, followed by $\langle g_\lambda\rangle$, $\langle g_\lambda\rangle^2$, $\langle g_\lambda\rangle^3$, $\langle g_\lambda\rangle^4$, and so on.

[33] For water clouds and aerosol particles it has been shown that the HG approximation produces very accurate radiative transfer model results for transmitted and reflected irradiances [e.g., *Hansen*, 1969]. However, in the case of cirrus clouds with extreme forward peaks of the phase function ($\theta < 2°$) this may no longer hold.

[34] To investigate this problem, the data from the optically thin cirrus case on 26 July have been used because effects due to the HG approximation are expected to be greatest for low-order scattering. Multiple scattering processes always tend to smooth out special features of the single-scattering optical properties. The reflected irradiance spectra above the cirrus at the flight level of the ER-2 and the transmitted spectral irradiance at the Twin-Otter flight altitude below the cloud have been calculated in two ways. (1) ''HG simulations'': The HG phase function was employed in the radiative transfer simulations using the asymmetry parameter from equation (3). (2) ''Exact simulations'': The exact volumetric phase function using equation (4) has been used in the radiative transfer calculations. Both approaches 1 and 2 were performed assuming columnar-shaped ice particles.

[35] For the exact simulations, $\langle p_\lambda\rangle$ has been expanded into 3000 Legendre-coefficients which assured an accurate representation over the entire range of scattering angles θ. In particular, the strong forward peak (at angles $\theta < 2°$) typical for ice crystals is hard to reproduce. However, nearly half of the scattered energy is concentrated in scattering angles less than 2°, one quarter below 0.4° and one tenth below 0.2°. Therefore much caution (i.e., thousands of Legendre-coefficients) is needed to accurately reproduce $\langle p_\lambda\rangle$ of ice crystals.

[36] The results of the calculations can be summarized as follows: For the reflected spectral radiation (400 nm $\leq \lambda \leq$ 1350 nm) above the cirrus, the ratio of the irradiance spectra calculated with the HG and the exact simulations was between +7% at 630 nm and −4% at λ = 1200 nm. For the transmitted irradiance below the cirrus this ratio was within ±1%. For wavelengths beyond 1350 nm larger deviations were obtained, especially within the ice absorption bands. We concluded that for the radiation below the cirrus the HG approximation is completely sufficient to reproduce accurately the radiative effects of cirrus clouds. The reflected radiation above the cirrus is more sensitive to the exact shape of the phase function, although there are no serious differences between the results of the HG and exact simulations.

[37] Therefore, considering the enormous computational efforts needed to accurately expand the exact volumetric phase function, in the following analysis the HG approximation has been used to calculate the irradiance spectra above and below the cirrus. By doing so an uncertainty of at maximum ±7% (outside the ice absorption bands) can be expected, which is slightly greater than the measurement uncertainty of the SSFR.

3. Influence of Cirrus Crystal Habits

[38] The radiation calculations were performed for the two cirrus cases (26 and 23 July) assuming the particle habits introduced at the beginning of subsection 2.2. For individual ice crystals, the impact of particle shape on single-scattering optical properties is discussed in subsection 3.1. The crystal shape sensitivity of the volumetric optical properties is analyzed in subsection 3.2. The irradiance spectra as a function of crystal shape are compared with the measurements of the SSFR in subsection 3.3. Subsection 3.4 shows the impact of the assumed crystal habits on the radiative forcing for the cirrus.

3.1. Single-Scattering Optical Properties of Individual Ice Crystals

[39] As an example, Figure 5 shows the spectral dependencies of the extinction cross section $C_{ext,\lambda}$ (Figure 5a), the asymmetry parameter g_λ (Figure 5b), and the single-scattering albedo ω_λ (Figures 5c and 5d) for mono-disperse ice crystals (fixed maximum dimension D = 25 μm) of different crystal habits.

[40] Clearly the spherical assumption yields the largest $C_{ext,\lambda}$ because spheres have the largest geometrical cross section for a fixed maximum particle dimension D. Con-

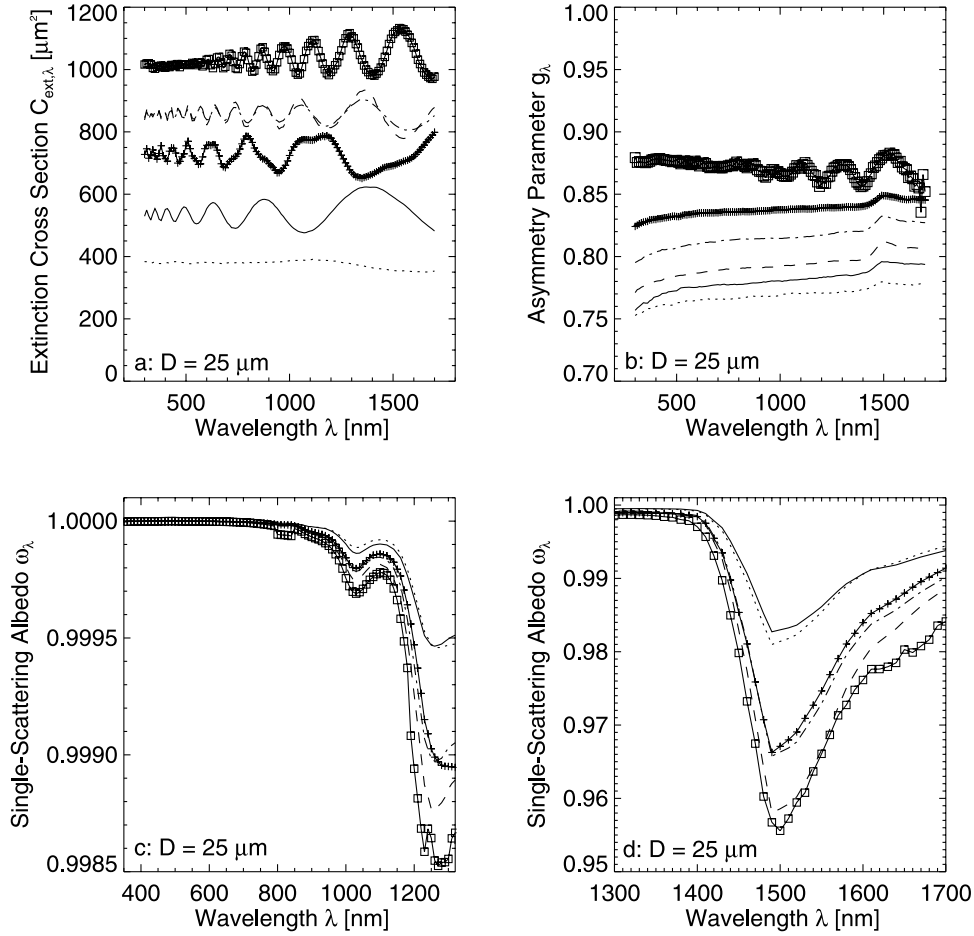

Figure 5. Individual ice crystals: (a) Extinction cross section $C_{ext,\lambda}$, (b) asymmetry parameter g_λ, and (c and d) single-scattering albedo ω_λ as a function of wavelength λ for ice crystals with a fixed maximum dimension of $D = 25$ µm. The curve notation is as follows: solid lines with open squares for spheres; dashed lines for columns; dash-dotted lines for hollows; solid lines with pluses for plates; solid lines for bullets; dotted lines for aggregates.

versely, aggregates exhibit the lowest values of $C_{ext,\lambda}$. Spheres also lead to the highest values of g_λ, while aggregates exhibit the largest deviations of the scattering pattern from the sphere evidenced by the lowest values for g_λ. There is only a slight wavelength dependence of g_λ for all crystal habits considered.

[41] Even weak ice crystal absorption may have a large impact on solar radiation due to the magnifying effect of multiple scattering. Therefore the plots for the calculated spectra of the single-scattering albedo ω_λ are split into two wavelength ranges: 350–1300 nm (Figure 5c) and 1300–1700 nm (Figure 5d). The two figures cover different vertical axis ranges and thus allow to depict in more detail the three major ice absorption bands (1030 nm; 1250 nm; and 1490 nm) in the SSFR spectral range. The single-scattering albedo is practically 1 for wavelengths less than about 800 nm, and drops within the ice absorption bands. ω_λ is anti-correlated with $C_{ext,\lambda}$; high extinction also results in high absorption, i.e. low values of ω_λ, and vice versa. Thus spheres exhibit the largest absorption (lowest values of ω_λ) because of the geometrical cross section is largest compared to all other crystal shapes. Aggregates and bullets show the weakest absorption and hence the largest ω_λ. The strongest differences among the different crystal shapes are within the ice absorption bands, reflecting differences in their respective radiative effective sizes.

[42] As another example, Figure 6 shows the same single-scattering optical properties at fixed wavelengths but as a function of maximum crystal dimension D. $C_{ext,\lambda}$ is clearly increasing with D with largest values for spheres, as expected, since it can be approximated as twice the geometric cross section in the geometric optics limit. g_λ has also a general tendency to increase with D and is very different for the crystal shapes investigated here. ω_λ decreases monotonically with increasing particle size in the ice absorption band of 1490 nm with an increasing crystal shape sensitivity toward larger particles.

[43] It is concluded that in terms of absorption crystal shape matters mainly in the ice absorption bands. Moreover, we conclude that the single-scattering albedo exhibits the expected increase with maximum particle dimension for all crystal habits but with considerable variability in magnitude due to shape dependencies on photon path lengths within the various crystal types. $C_{ext,\lambda}$ and g_λ are strongly influenced by the crystal shape assumption

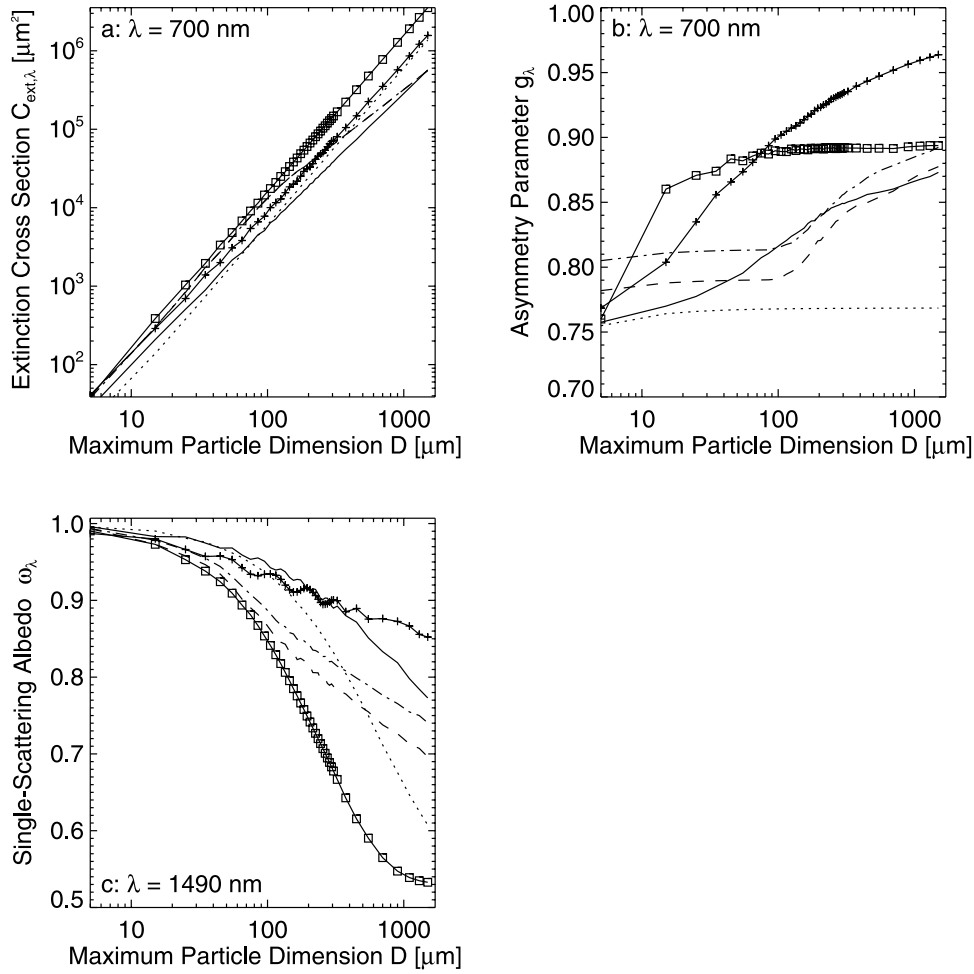

Figure 6. Individual ice crystals: (a) Extinction cross section $C_{ext,\lambda}$, (b) asymmetry parameter g_λ, and (c) single-scattering albedo ω_λ as a function of maximum particle dimension D for a fixed wavelength of λ = 700 nm (Figures 6a and 6b) and within the ice absorption band of λ = 1490 nm (Figure 6c). The curve notation is the same as in Figure 5.

throughout the entire solar wavelength range and for all crystal sizes.

3.2. Volumetric Optical Properties of Ice Crystal Populations

[44] Figure 7 shows an example of the results of the calculations for the cirrus cloud observed on 23 July. Displayed are the profiles of the volume extinction coefficient $\langle b_{ext,\lambda}\rangle$ (Figure 7a), the volumetric asymmetry parameter $\langle g_\lambda\rangle$ (Figure 7b), and the volumetric single-scattering albedo $\langle \omega_\lambda\rangle$ (Figure 7c) for the different particle habits. In Figure 7a the curves for columns and hollows are almost identical, therefore only the columns are plotted. The measured volume extinction coefficient $b_{ext,vis}$, as derived from the CAPS/SPP/CPI instruments, is added to Figure 7a as a solid line with open diamonds.

[45] The profile of $\langle b_{ext,\lambda}\rangle$ closely follows the vertical pattern of the microphysical measurements on that day (Figure 4). $\langle b_{ext,\lambda}\rangle$ is linked to $C_{ext,\lambda}$ via equation (1). Therefore, similar to Figures 5a and 6a, $\langle b_{ext,\lambda}\rangle$ for spheres is much larger compared to all other particle shapes because spheres yield the largest cross section for a given maximum particle dimension. The extinction is lowest for aggregates which, conversely, yield the smallest cross section per maximum particle dimension. There is a considerable spread between the curves (about 60%), which shows the significant influence of ice crystal shape on volumetric extinction.

[46] Both, the profiles of $\langle g_\lambda\rangle$ and $\langle \omega_\lambda\rangle$ are nearly constant with altitude through most of the cloud. $\langle g_\lambda\rangle$ is largest for spheres and lowest for aggregates, in correspondence with Figures 5b and 6b. As for the single-scattering optical properties, $\langle \omega_\lambda\rangle$ is anti-correlated with $\langle b_{ext,\lambda}\rangle$. The range of magnitude of $\langle g_\lambda\rangle$ and $\langle \omega_\lambda\rangle$ for the different shape assumptions is approximately 10%.

[47] From the calculated profiles of the volume extinction coefficient the optical thickness of the cirrus clouds τ_λ was calculated for the different crystal habits by

$$\tau_\lambda = \int \langle b_{ext,\lambda}(z')\rangle \cdot dz'. \quad (6)$$

The resulting calculated τ_λ at 700 nm wavelength for the two cloud cases considered here is given in Table 2. Spheres

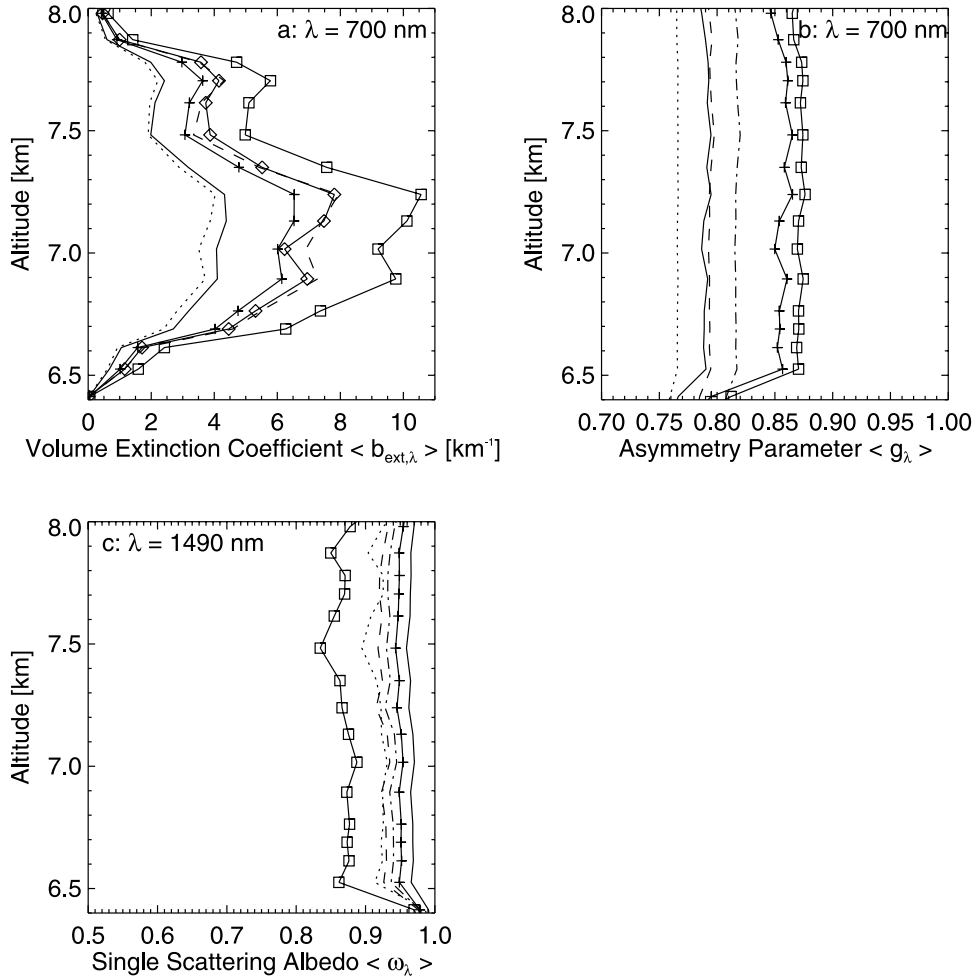

Figure 7. Ice crystal populations: Profiles of the (a) volume extinction coefficient $\langle b_{ext,\lambda} \rangle$, (b) asymmetry parameter $\langle g_\lambda \rangle$, and (c) single-scattering albedo $\langle \omega_\lambda \rangle$ at a wavelength of $\lambda = 700$ nm (Figures 7a and 7b) and in the ice absorption band at $\lambda = 1490$ nm (Figure 7c). The curve notation is the same as in Figure 5. Additionally the volume extinction coefficient $b_{ext,vis}$ as derived from the CAPS/SPP/CPI instruments is included (solid lines with open diamonds in Figure 7a). The size distribution data have been taken on 23 July (cirrus of moderate optical thickness).

(aggregates) result in the largest (smallest) optical thickness which follows from Figure 7a. This conclusion is valid for both cases, 26 and 23 July.

3.3. Downwelling and Upwelling Irradiance Spectra

3.3.1. Optically Thin Cirrus

[48] Figure 8 shows the measured (solid lines) and calculated downwelling and upwelling irradiance spectra for the flight level of the ER-2 above the cloud assuming a columnar particle shape in the calculations. The measured downwelling irradiance spectra $F_\lambda^\downarrow$ in Figure 8a agree with the calculations within ±5% (for $\lambda \geq 400$ nm), which is within the instrument measurement uncertainty. The ratio of measured to calculated spectra of $F_\lambda^\downarrow$ above the cloud is practically independent of the assumed ice crystal shape (not shown). Downwelling irradiance spectra above the cloud are neglibly influenced by the cloud layer beneath.

[49] The calculated upwelling irradiances $F_\lambda^\uparrow$ shown in Figure 8b are systematically lower than the measured irradiances but, nevertheless, are within the variability of the measurements over the flight track (vertical bars). The ratio of measured and calculated $F_\lambda^\uparrow$ is about 10% in the UV-VIS spectral range ($\lambda \leq 1000$ nm) for the columnar crystal shape assumption. For the NIR wavelength range this ratio may reach values of ±50%. Crystal shape assumptions other than

Table 2. Spectral Optical Thickness τ_λ of the Cirrus Cloud Layers for $\lambda = 700$ nm Wavelength, as Derived From the Calculations (Equation (6)) Assuming Different Ice Crystal Shapes

	26 July 2002 Optically Thin Cirrus	23 July 2002 Cirrus of Moderate Optical Thickness
Spheres	1.5	9.2
Columns	1.2	6.6
Hollows	1.2	6.6
Plates	0.87	5.7
Bullets	0.57	3.7
Aggregates	0.53	3.4

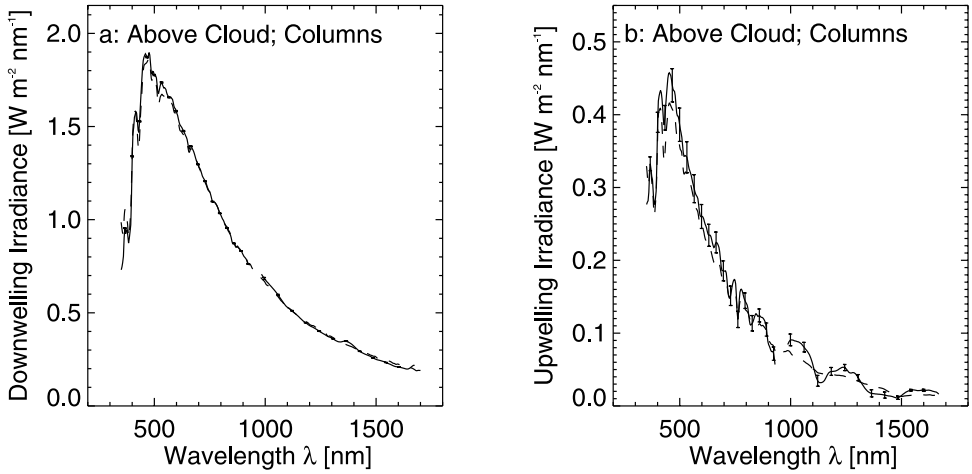

Figure 8. Measured (solid lines, ER-2) and calculated (dashed lines) (left) downwelling irradiance $F_\lambda^\downarrow$ and (right) upwelling irradiance $F_\lambda^\uparrow$ for the flight level of the ER-2 (19.9 km) above the cloud for 26 July (optically thin cirrus). The measurements are averaged along the flight track; the vertical bars represent the standard deviations of the measurements along the flight track. The average solar zenith angle for the ER-2 measurements, $\theta_s = 21°$, was used in the radiative transfer simulations. Columns have been assumed as ice crystal shapes.

columns yield larger deviations between measured and calculated $F_\lambda^\uparrow$ above the cloud (not shown). However, the absolute differences between measurements and calculations are quite small (0.04 W m^{-2} nm^{-1} at λ = 500 nm) because little radiation is reflected by this optically thin cirrus cloud. Therefore, small systematic errors, for example, those associated with absolute calibration (offsets) may cause large relative deviations, but the effects on total solar radiation energy is minimal. Additionally, uncertainties in the microphysical measurements can easily explain the measurement-model differences in the reflected irradiance above the cloud. However, it is not the objective of this paper to study the sensitivity of scattered irradiance with respect to microphysical measurement uncertainties. Moreover, for this special case of optically thin cirrus, uncertainties in the surface albedo, and possible contamination by low clouds may play a role. Such low clouds are not considered in the radiative transfer calculations and may have increased the measured reflected irradiance above the cloud.

[50] The promising agreement between measured and calculated irradiance spectra (both downwelling and upwelling) assuming a columnar crystal shape does not necessarily lead to the conclusion that this crystal habit was dominant in the cirrus cloud on 26 July. There are too many uncertainties (microphysical measurements, surface albedo, low cloud below the cirrus) in the simulations. The variation of these variables within their range of uncertainty, which has not been attempted in this paper in detail, may lead to other favored crystal shapes. For example, using the CAPS/SPP/CPI composite crystal size distributions yields systematically lower reflected irradiance spectra in the VIS (about 5%) and slightly higher values in the NIR, compared to the calculations based on the VIPS size distributions in this optically thin cirrus case. The CAPS/SPP/CPI size distributions are systematically larger for $D \leq 25$ μm, and lower for $D > 25$ μm than the VIPS data. Also the VIPS data do not include ice crystals with $D > 300$ μm. Therefore it is not surprising that the resulting reflected irradiance spectra are different for the two microphysical data sets. In spite of these issues, the general agreement between measurements and calculations shows that the observed radiation can be explained using measured model input, even in this complicated case of an optically thin cirrus cloud.

[51] Figure 9 shows the ratio of calculated upwelling irradiance spectra for each of the nonspherical habits to that for spheres at the ER-2 flight level. On the basis of Figure 7a it might be expected that the spheres would yield the highest reflected irradiance and thus should be on either of the extremes in the curve family in Figure 9. Instead, spheres lie somewhat in the midrange of the curves. This is because, even though spheres exhibit the largest $\langle b_{ext,\lambda} \rangle$, they are also characterized by the largest $\langle g_\lambda \rangle$ values. These competing effects may lead to greater (due to the large $\langle b_{ext,\lambda} \rangle$) or less (due increased forward scattering as indicated by higher $\langle g_\lambda \rangle$ values) reflected radiation depending upon the relative strength of these effects compared to those of the various nonspherical habits.

[52] Figure 9 exhibits considerable variability with wavelength for this cirrus case. For λ = 400 nm it does not really matter which shape is assumed in the calculations. The relative spread spanned by the curves (i.e. the percentage difference between the solid line with pluses for plates and the dashed line for columns) is about 13% for λ = 400 nm. It increases with wavelength to a maximum value of about 100% for λ = 1400 nm. Within the gas absorption bands of H_2O and O_2 the curves diverge, within the ice absorption bands (1030 nm; 1250 nm; and 1490 nm) the curves converge.

[53] The optically thin cirrus case occurred during high solar elevation (small value of solar zenith angle $\theta_s = 21°$). For near-zenith incidence the majority of incident photons encounter only one scattering event for a cloud of this optical depth ($\tau_{vis} \approx 1$). For low solar elevation (larger solar zenith angle) the slant path through the cloud is significantly

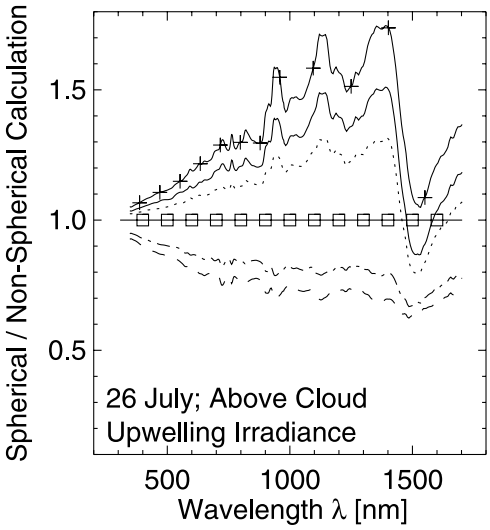

Figure 9. Ratio of calculated upwelling irradiance $F^{\uparrow}_{\lambda}$ assuming spherical and nonspherical ice crystal shapes for the flight level of the ER-2 (19.9 km) above the cloud for 26 July (optically thin cirrus). The solar zenith angle was $\theta_s = 21°$. The curve notation is the same as in Figure 5.

enhanced and thus the probability of multiple scattering increases. One may expect then that some of the distinct characteristics of the nonspherical single-scattering optical properties would diminish at larger solar zenith angles. Indeed, additional calculations have shown this to be true. In these calculations θ_s was increased to 75°. A plot similar to that shown in Figure 9 was produced (not shown). In this plot the relative spread spanned by the resulting curve family decreased from 13% (for $\theta_s = 21°$) to 4% (for $\theta_s = 75°$) at $\lambda = 400$ nm. The ratio range at $\lambda = 1400$ nm decreased to about 36% (from 100% for $\theta_s = 21°$). This shows that, as expected, the crystal shape sensitivity of the reflected irradiance spectra above the cloud was reduced with increasing θ_s, due to the increased multiple scattering which tends to diminish shape characteristics caused by nonspherical single-scattering. It should be noted that relative differences of the volumetric phase function as a function of scattering angle (among the various ice crystal shapes) may also contribute to the solar incident angle dependence.

3.3.2. Cirrus of Moderate Optical Thickness

3.3.2.1. Irradiance Above the Cloud

[54] Figure 10 shows the comparison between observed and simulated downwelling and upwelling irradiance spectra above the cirrus for the 23 July case. The calculation using aggregates led to the best agreement with the measurements and are shown here. Because the solar zenith angle was much larger in this case ($\theta_s = 78°$), the downward irradiance in Figure 10a is lower compared to Figure 8a. The cloud observed on 23 July was optically thicker compared to the case described in subsection 3.3.1, and therefore the reflected irradiance above the cloud shown in Figure 10b is higher (relative to the downward irradiance) than for the 26 July case shown in Figure 8b. The ratio of measured to calculated downwelling irradiance spectra is similar to that for the optically thin cloud case (within ±5%). The ratio of the upwelling irradiance spectra above this cloud is also within ±5%, which is even lower than for the optically thin cloud case. This improved agreement between measured and calculated upwelling irradiance above the cloud (compared to the optically thin cirrus case) likely results from factors such as a smaller contribution from the surface albedo variations along the flight track to the above-cloud upwelling irradiance as well as from other scatterers in the lower atmosphere such as low clouds. For these reasons this thicker cirrus might be considered less complicated than the optically thin cirrus case, at least in a radiative sense.

[55] The downwelling irradiance above the optically thicker cirrus on 23 July was practically insensitive to the chosen crystal shape, similar to the case of optically thin cirrus. The agreement between measured and calculated upwelling irradiance spectra at the ER-2 flight level was less than that of the downwelling irradiance spectra for all habits except aggregates. The poorest agreement was found

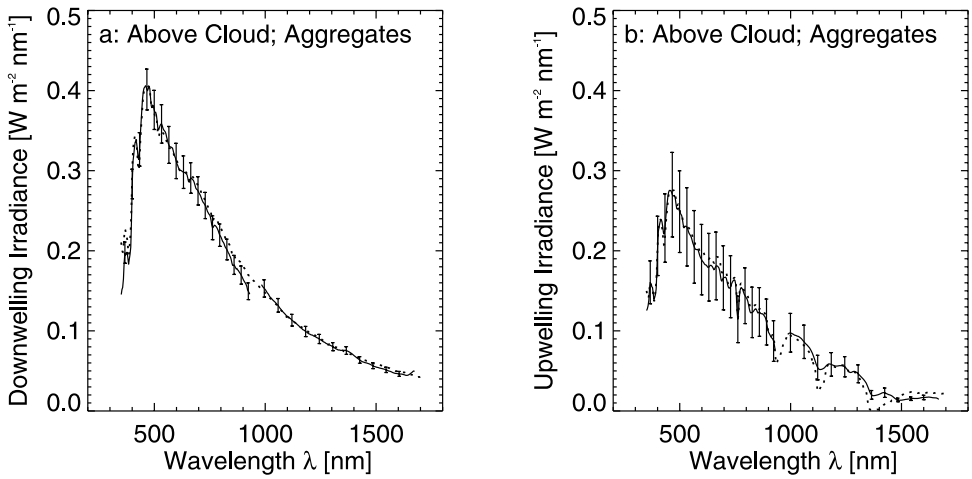

Figure 10. Same as Figure 8, but for the measurements taken on 23 July (flight level of the ER-2: 20.7 km; $\theta_s = 78°$). In the calculations (dotted lines), aggregates have been assumed as ice crystal shapes.

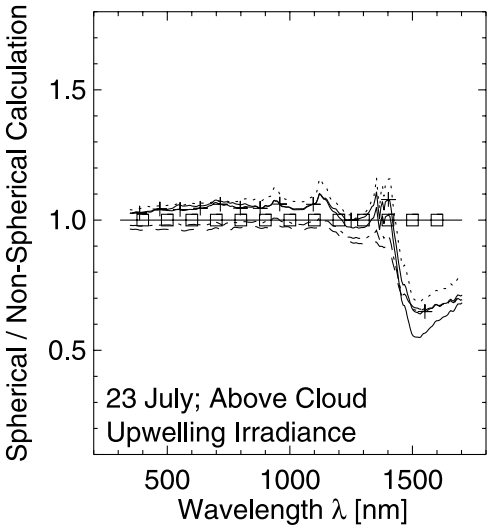

Figure 11. Same as Figure 9, but for 23 July (flight level of the ER-2: 20.7 km; $\theta_s = 78°$). The curve notation is the same as in Figure 5.

for columns. However, the ratio of measured to calculated reflected irradiance in the worst case was still less than 10% (outside the gas and ice absorption bands) and thus clearly within the standard deviation of the observed upwelling irradiance spectra over the flight ER-2 track.

[56] This implies that for this case of an optically thicker cirrus cloud the general sensitivity of the reflected irradiance with regard to crystal shape is smaller compared to the optically thinner cloud case on 26 July. This fact further emphasizes the influence of multiple scattering on reducing the variability seen in the single-scattering characteristics of the various crystal habits. This is quantified in Figure 11, which shows that the spread between the curves is smaller than 10–20% throughout the entire spectral range of the SSFR. Even the most unlikely of crystal shape, spherical, can sufficiently reproduce the observed spectra at wavelengths less than 1400 nm within the variability of the measurements over this time period. For larger wavelengths, however, effects due to crystal shape become more significant and this is due to the variability in single-scattering albedo evident in Figures 5c and 5d. For multiple scattering media these absorption effects are further amplified. This is a fundamental difference between the nonsphericity effects on atmospheric scattering and absorption. Enhance multiple scattering smoothes out the nonsphericity effects for wavelengths where scattering dominates, but amplifies the nonsphericity impact within the ice absorption bands.

[57] If the solar zenith angle is artificially decreased from $\theta_s = 78°$ (as it was the case during the actual measurement) to $\theta_s = 15°$, then the span of the curves increases to a maximum of ±20% (not shown) due to less multiple scattering. Therefore it is concluded that the influence of the crystal shape assumed in the calculations on reflected irradiance above cirrus clouds of moderate optical thickness is only significant for small zenith angles. For clouds with larger optical thickness, this influence is expected to become negligible.

[58] From this comparison it is concluded that the reflected irradiance above the cirrus cloud with moderate optical thickness can be reproduced by the calculations within its natural variability. The sensitivity to particle shape, however, is too low to allow a determination of the habit from this kind of measurement. Even spherical particle shapes lead to a reasonable agreement between measured and calculated reflected irradiance.

3.3.2.2. Irradiance Below the Cloud

[59] Below the cirrus cloud the comparison between measured and calculated irradiance was not satisfactory (see Figure 12). The simulated downwelling and upwelling irradiance spectra clearly exceeded the range of variability in the measurements along the flight track (vertical bars; note that these are considerably larger than measurement uncertainty which is the range of 4–6% across the spectrum). For the downwelling irradiance the calculations are about 50% lower compared to the measurements, while the upwelling irradiance deviates even more (200–500%).

[60] Part of the upwelling irradiance is directly proportional to the surface albedo. A good estimate of the surface albedo is therefore crucial for the calculation of the upwelling irradiances below cloud. However, also the simulation of the downwelling irradiance below the highly reflecting cloud base is influenced by the surface albedo. In the calculations presented in Figure 12 the sea surface albedo measured during the CRYSTAL-FACE campaign was used [*Wendisch et al.*, 2004]. However, parts of the flight track were over land surface (see Figure 3). Indeed, an increase in the upwelling irradiance spectra for wavelengths larger than 700 nm (vegetation step) was evident in Figure 12b, and this is a typical feature of land surface vegetation. Therefore the calculations were repeated using the respective land surface albedo data by *Wendisch et al.* [2004], which were also collected during CRYSTAL-FACE. This improved the measurement-calculation comparison but it did not completely remove the discrepancy between measurement and model. Clearly additional factors contributed to the differences between measured and calculated downwelling and upwelling irradiance spectra below the cirrus cloud on 26 July.

[61] The microphysical measurements from the WB-57F were taken outside the immediate vicinity of the flight tracks of the ER-2 and the Twin Otter (see Figure 3). The Lidar backscattering measurements taken on board the ER-2 have revealed significant variability of the cloud structure along the flight track (M. McGlill, personal communication). Therefore it seems likely that the one-dimensional microphysical measurements of the WB-57F do not fully represent the cloud field in this specific case. For the ER-2 (flying at 20.7 km altitude) the radiation measurements were collected well above the cloud top (8.0 km). Therefore problems associated with cloud spatial inhomogeneities are less crucial, simply because the spatial variability is smoothed out by the angular integration of hemispheric measurements made several kilometers above cloud top. The Twin-Otter was flying at 3.6 km altitude, much closer to the cloud base (6.4 km) than the ER-2. Furthermore the flight track of the Twin-Otter was shorter. Therefore, with the additional complications of variable land surface albedo (and part of the track was over

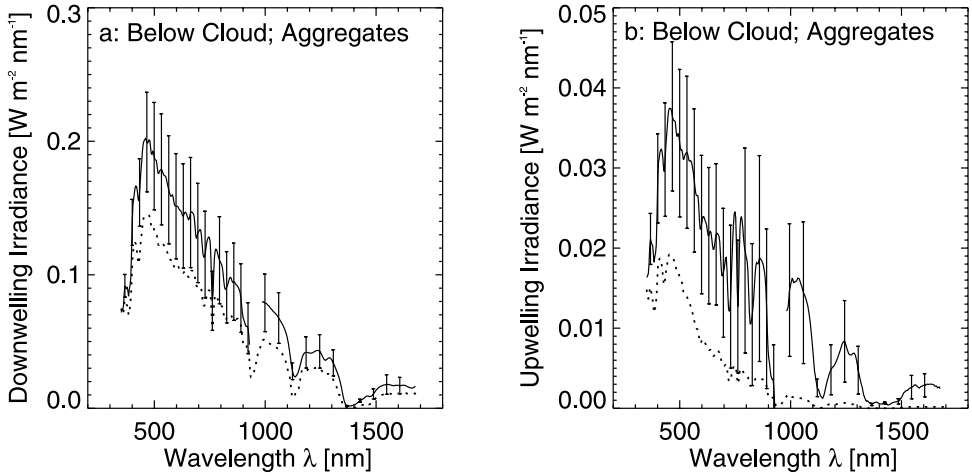

Figure 12. Measured (solid lines, Twin-Otter) and calculated (dotted lines) (left) downwelling irradiance $F_\lambda^\downarrow$ and (right) upwelling irradiance $F_\lambda^\uparrow$ for the flight level of the Twin-Otter (3.6 km) below the cloud (θ_s = 78°). The measurements are averaged along the flight track; the vertical bars represent the standard deviations of the measurements along the flight track. In the calculations, aggregates have been assumed as ice crystal shapes. The data have been taken on 23 July (cirrus of moderate optically thickness).

sea), cloud inhomogeneities lead to significant deviations between measured and calculated irradiance spectra below the cloud.

[62] Below the cloud the shape sensitivity of the downwelling irradiance spectra is larger (see Figure 13) compared to that of the reflected irradiance above the cloud (Figure 11). The span of the curves is ≈25%. Serious deviations from the spherical shape assumption are apparent at wavelengths larger than 1000 nm.

[63] The dependence of the ratio shown in Figure 13 on the solar zenith angle is small. Respective calculations for θ_s = 15° (not shown) are nearly identical to the results for θ_s = 78° (as shown in Figure 13) with a slightly decreased span of the curves and somewhat lower deviations of the nonspherical calculations to those obtained by the spherical shape assumption. Below the cloud with only diffuse irradiance the photons loose the memory of their source direction. The slightly decreased sensitivity to shape assumptions for smaller θ_s values is a result of the lower photon path lengths and, therefore, less frequent multiple scattering interactions of the photons penetrating the cloud for high Sun.

3.4. Cirrus Radiative Forcing

[64] Solar radiative forcing is a good quantitative indicator of the climatic impact of cirrus clouds. To derive this quantity the solar spectral radiative forcing (in units of W m^{-2} nm^{-1}) of the cirrus clouds at the flight level of the ER-2 (z_{top}) was calculated by

$$\triangle F_{top,\lambda} = F^{\uparrow}_{clear,\lambda}(z_{top}) - F^{\uparrow}_{cloudy,\lambda}(z_{top}), \qquad (7)$$

with index "clear" indicating cloud-free and the index "cloudy" for the case when clouds were included in the calculations. $\triangle F_{top,\lambda}$ is practically identical to the radiative forcing of the cirrus clouds at the top of atmosphere. Integration of the spectral forcing over the wavelength range of the SSFR yields the solar integrated radiative forcing (in units of W m^{-2}) of the cirrus. Although the spectral range of the SSFR does not cover the entire solar spectrum, the integrated cirrus radiative forcing is almost very close to the total solar radiative forcing.

[65] The effects of crystal shape assumptions on the calculated solar spectral radiative forcing of the cirrus cloud observed on July 23 has been investigated (Figure 14). For θ_s = 78° (Figure 14a) the influence of the shape assumption seems to be of minor importance. The ratio of spherical to nonspherical forcing (Figure 14b) is mostly less than ±10%

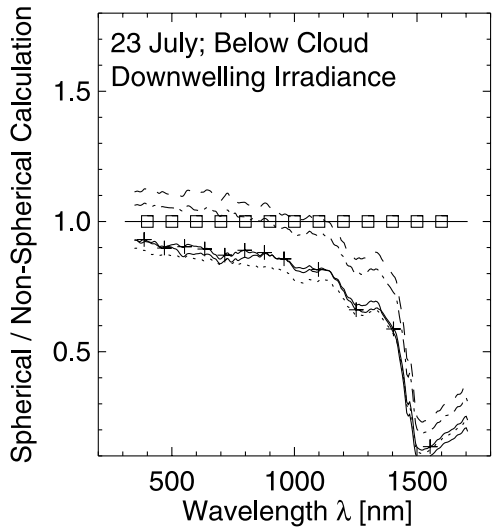

Figure 13. Ratio of calculated downwelling irradiance $F_\lambda^\downarrow$ assuming spherical and nonspherical ice crystal shapes for the flight level of the Twin-Otter (3.6 km) below the cloud (θ_s = 78°). The data have been taken on 23 July (cirrus of moderate optical thickness). The curve notation is the same as in Figure 5.

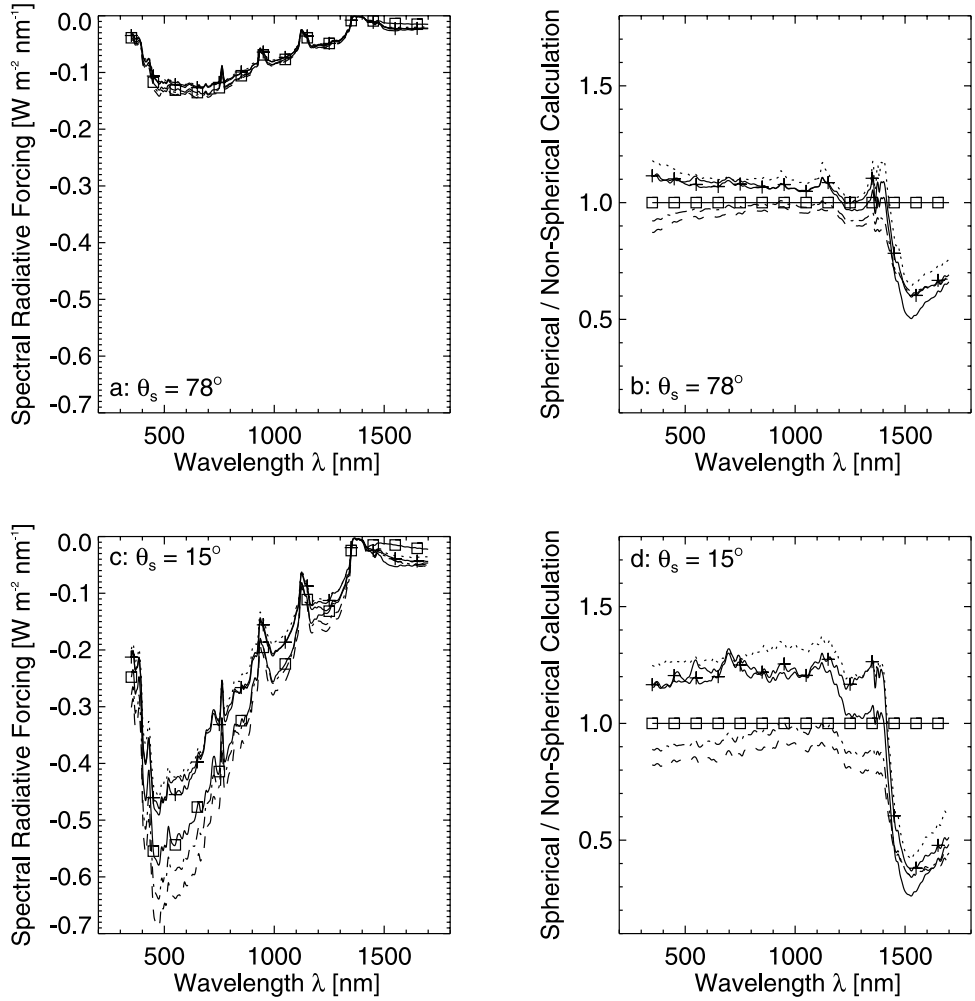

Figure 14. Spectral radiative forcing as calculated from microphysical data taken on 23 July (cirrus of moderate optical thickness). (a) Forcing is calculated for a solar zenith angle of $\theta_s = 78°$. (c) Calculations are performed for $\theta_s = 15°$. (b and d) Spectral ratio of the calculated radiative forcing of the cirrus assuming spheres and nonspherical crystal habits. The curve notation is the same as in Figure 5.

for $\lambda \leq 1400$ nm. For larger wavelengths within the major ice absorption band nonspherical simulations deviate significantly from spheres. For a smaller solar zenith angle ($\theta_s = 15°$) the calculations yield much higher absolute spectral cloud forcing (Figure 14c), because the incoming solar radiation is higher. Owing to less multiple scattering for high Sun, the shape effects are significantly greater (Figure 14d) than the lower Sun counterparts.

[66] The total (spectrally integrated) cirrus radiative forcing for each of the crystal shapes are listed in Table 3. For $\theta_s = 78°$ nonspherical shapes make a maximum change in forcing of approximately ±8%. For $\theta_s = 15°$ (i.e., less multiple scattering) the relative influence of the crystal shape chosen in the calculations is much higher (between −16% for columns and +26% assuming aggregates). This clearly shows that crystal shape matters for the calculation of the solar radiative forcing of the cirrus cloud investigated here.

4. Summary and Conclusions

[67] In this paper two cirrus cloud cases (26 July 2002: optically thin cloud with $\tau_{vis} \approx 1$; and 23 July 2002: cirrus of moderate optical thickness with $\tau_{vis} \approx 7$) from the CRYSTAL-FACE were analyzed in terms of their microphysical and radiative properties. One objective was to investigate how well measured irradiance spectra and spectral cirrus optical properties could be reproduced by radiative transfer calculations using actual crystal size distribution measurements. In other words, how well could microphysical aircraft measurements be used to represent the spectral irradiance above and below the cirrus. The second, major goal of this paper was to quantify the influence of different crystal habits on (1) the spectral single-scattering optical properties of individual ice crystals, (2) the volumetric optical properties of populations of crystals, (3) the downwelling and upwelling irradiance spectra above and below the clouds, and (4) the spectral and solar radiative forcing of the cirrus clouds investigated.

[68] Data from instruments on board three aircraft (NASA ER-2 and WB-57F, CIRPAS Twin Otter) were used in this study. Microphysical measurements (ice crystal size distributions) were conducted by the VIPS and CAPS/SPP/CPI instruments mounted on the WB-57F

Table 3. Spectrally Integrated (Solar) Radiative Forcing of the Cloud Investigated During CRYSTAL-FACE on 23 July 2002 (Cirrus of Moderate Optical Thickness)

	$\theta_s = 78°$ Solar Radiative Forcing, W m^{-2}	$\theta_s = 78°$ Sphere/Nonsphere	$\theta_s = 15°$ Solar Radiative Forcing, W m^{-2}	$\theta_s = 15°$ Sphere/Nonsphere
Columns	−100	0.928	−377	0.844
Hollows	−96	0.955	−348	0.913
Spheres	−93	1	−318	1
Bullets	−89	1.042	−272	1.168
Plates	−89	1.044	−269	1.180
Aggregates	−86	1.082	−253	1.257

aircraft. The radiation data were collected by the NASA SSFR, which measures spectral downwelling and upwelling irradiance in the wavelength range from 350–1670 nm. Two identical versions of the SSFR were installed on the Twin Otter and ER-2 aircraft. The ER-2 measured the spectral downwelling and upwelling irradiance spectra above the cloud, the Twin-Otter collected radiation data below the cirrus.

[69] Single-scattering optical properties for individual ice crystals were calculated assuming several crystal shapes (spheres, columns, hollows, plates, bullets, aggregates). These results were combined with the measured profiles of the crystal size distributions to calculate the vertical distribution of the spectral volumetric optical properties of the ice crystal populations (volume extinction coefficient, volumetric single-scattering albedo, volumetric asymmetry parameter), which subsequently were used as input in spectral radiative transfer calculations.

[70] The measured and calculated downwelling and upwelling solar irradiance spectra above the cirrus were in close agreement (mostly within ±5–10%) for most of the assumed crystal habits. Below the cirrus the measured and calculated irradiance agreement was poorer, most likely because of highly variable surface albedo and nonideal coincidence in time and space between the microphysical and radiation measurements. The impact of nonspherical crystal shapes on the reflected irradiance spectra above the cirrus was significant for the optically thin cloud case on 26 July. For the optically thicker cirrus case on 23 July, this effect was significant only for small solar zenith angles. For cirrus with larger optical thickness, this influence is expected to become negligible. Below the cirrus the impact of the crystal habit on downwelling irradiance was found to be larger than for the reflected irradiance above the cirrus. In general it was shown that, outside the ice absorption bands, the impact of nonsphericity is more and more diminished if multiple scattering (due to higher cloud optical thickness, or larger solar zenith angle which means a larger photon path length) becomes dominant. Whereas multiple scattering smoothes out the nonsphericity effects outside the ice absorption bands, it magnifies the impact of nonspherical ice crystal shape within the ice absorption bands.

[71] The effects of crystal shape on the calculated solar spectral radiative forcing of the cirrus cloud observed on 23 July were small (within ±10%) for large solar zenith angles. For smaller solar zenith angles the shape effects became significant. The spectrally integrated cirrus radiative forcing for the different crystal shapes was also investigated. For large solar zenith angles the nonspherical shapes had a maximum effect of roughly ±8%; for small solar zenith angles the relative influence of the crystal shape increased (maximum values between −16% and +26%).

[72] The results presented in this paper identify some problems related to colocation of the microphysical and radiation measurements. Because cirrus clouds, by their nature, are spatially and temporarily inhomogeneous, aircraft measurements along a single flight track cannot fully represent the microphysical input needed for the radiative transfer simulations. The aircraft data are snapshots through the clouds and the exceptionally good agreement between measured and calculated reflected irradiance spectra above the clouds reported here could have been the result of luck. Therefore one lesson we have learned from this work is that cloud microphysical temporal and spatial inhomogeneity has to be considered and characterized much more carefully than is possible with aircraft observations alone. Problems arise, even when aircraft are perfectly colocated. Microphysical aircraft data are like random needle peaks in the cloud. They should be complemented by remote sensing techniques such as Lidar or radar.

[73] In a related study to this paper (P. Pilewskie et al., manuscript in preparation, 2005), ice crystal effective radius and cirrus optical thickness are retrieved from SSFR spectral irradiance using a modified version of the single-scattering library [*Yang et al.*, 2000] used in the present paper. The radiatively dominant effective ice crystal size was found to be in close agreement to retrieved quantities from the Moderate Resolution Imaging Spectrometer (MODIS) Airborne Simulator, which also flew on the ER-2 during CRYSTAL-FACE. However, the magnitude of ice crystal sizes determined by remote sensing was considerably larger than values derived from in situ measurements of bulk *IWC* and cirrus extinction [*Garrett et al.*, 2003] and this emphasizes the complexity of relating the radiative, microphysical, and bulk measurement of cirrus clouds from airborne platforms. These discrepancies need to be resolved in order to improve our understanding of the relationship between ice crystal microphysical properties and cirrus radiative properties which will ultimately lead to improved modeling of cirrus clouds in the context of the global climate system.

[74] **Acknowledgments.** This research was performed while one of the authors (M.W.) held a National Research Council Research Associateship Award at the NASA ARC. Jost Heintzenberg (IfT) has supported the 1-year stay of M.W. at ARC. We are grateful to Warren Gore, Larry Pezzolo, and Tony Trias (NASA ARC) for their engineering and technical support during CRYSTAL-FACE. We also wish to thank the NASA Earth Science Enterprise

Radiation Science Program for supporting this research. Steven Platnick is thanked for his thorough review of the manuscript. Stefan Kinne made helpful suggestions to improve the earlier paper version.

References

Anderson, G. P., S. A. Clough, F. X. Kneizys, J. H. Chetwynd, and E. P. Shettle (1986), AFGL atmospheric constituent profiles (0–120 km), *Air Force Geophys. Lab. Tech. Rep., AFGL–TR–86–0110*.

Baran, J., S. Haveman, P. N. Francis, and P. Yang (2001), A study of the absorption and extinction properties of hexagonal ice columns and plates in random and preferred orientation, using exact T-matrix theory and aircraft observations of cirrus, *J. Quant. Spectrosc. Radiat. Transfer*, *70*, 505–518.

Baumgardner, D., H. Jonsson, W. Dawson, D. O'Connor, and R. Newton (2002), The cloud, aerosol, and precipitation spectrometer: A new instrument for cloud investigations, *Atmos. Res.*, *59–60*, 251–264.

Francis, P. N., J. S. Foot, and A. J. Baran (1999), Aircraft measurements of the solar and infrared radiative properties of cirrus and their dependence on ice crystal shape, *J. Geophys. Res.*, *104*, 31,685–31,695.

Garrett, T. J., H. Gerber, D. G. Baumgardner, C. H. Twohey, and E. M. Weinstock (2003), Small, highly reflective ice crystals in low-latitude cirrus, *Geophys. Res. Lett.*, *30*(21), 2132, doi:10.1029/2003GL018153.

Gosse, S., D. Labrie, and P. Chylek (1995), Refractive index of ice in the 1.4 to 7.8 μm spectral range, *Appl. Opt.*, *34*, 6582–6586.

Hansen, J. E. (1969), Exact and approximate solutions for multiple scattering by cloudy and hazy planetary atmospheres, *J. Atmos. Sci.*, *26*, 478–487.

Heymsfield, A. J., and G. M. McFarquhar (1996), On the high albedos of anvil cirrus in the tropical Pacific warm pool: Microphysical interpretations from CEPEX and from Kwajalein, Marshall Islands, *J. Atmos. Sci.*, *53*, 2424–2451.

Jensen, E., D. Starr, and O. B. Toon (2004), Mission investigates tropical cirrus clouds, *Eos Trans. AGU*, *85*, 45–49.

Kinne, S., and K. N. Liou (1989), The effects of nonsphericity and size distribution of ice crystals on the radiative properties of cirrus clouds, *Atmos. Res.*, *24*, 273–284.

Liou, K.-N. (1986), Influence of cirrus clouds on weather and climate processes: A global perspective, *Mon. Weather Rev.*, *114*, 1167–1199.

Liou, K. N., Y. Takano, and P. Yang (2000), Light scattering and radiative transfer by ice crystal clouds: Applications to climate research, in *Light Scattering by Nonspherical Particles: Theory, Measurements, and Applications*, edited by M. I. Mishchenko, J. W. Hovenier, and L. D. Travis, chap. 15, pp. 417–449, Elsevier, New York.

Lynch, D. K., K. Sassen, D. O. Starr, and G. Stephens (Eds.) (2002), *Cirrus*, Oxford Univ. Press, New York.

Macke, A., P. N. Francis, G. M. McFarquhar, and S. Kinne (1998), The role of ice particle shapes and size distributions in the single scattering properties of cirrus clouds, *J. Atmos. Sci.*, *55*, 2874–2883.

Mayer B., and A. Kylling (2005), Technical Note: The libRadtran software package for radiative transfer calculations: Description and examples of use, *Atmos. Chem. Phys. Disc.*, in press.

Mishchenko, M. I., W. B. Rossow, A. Macke, and A. A. Lacis (1996), Sensitivity of cirrus cloud albedo, bidirectional reflectance, and optical thickness retrieval accuracy to ice particle shape, *J. Geophys. Res.*, *101*, 16,973–16,985.

Mitchell, D. L. (2002), Effective diameter in radiation transfer: General definition, applications, and limitations, *J. Atmos. Sci.*, *59*, 2330–2346.

Pilewskie, P., J. Pommier, R. Bergstrom, W. Gore, S. Howard, M. Rabbette, B. Schmid, P. V. Hobbs, and S. C. Tsay (2003), Solar spectral radiative forcing during the Southern African Regional Science Initiative, *J. Geophys. Res.*, *108*(D13), 8486, doi:10.1029/2002JD002411.

Ramaswamy, V., and V. Ramanathan (1989), Solar absorption by cirrus clouds and the maintenance of the tropical upper troposphere thermal structure, *J. Atmos. Sci.*, *46*, 2293–2310.

Sherwood, S. C. (1999), On moistening of the tropical troposphere by cirrus clouds, *J. Geophys. Res.*, *104*, 11,949–11,960.

Shettle, E. P. (1989), Models of aerosols, clouds, and precipitation for atmospheric propagation studies, *AGARD Conf.*, *454*.

Slingo, A. (1990), Sensitivity of the Earth's radiation budget to changes of low clouds, *Nature*, *343*, 49–51.

Stamnes, K., S. C. Tsay, W. Wiscombe, and K. Jayaweera (1988), A numerically stable algorithm for discrete-ordinate-method radiative transfer in multiple scattering and emitting layered media, *Appl. Opt.*, *27*, 2502–2509.

Tsay, S.-C., P. M. Gabriel, M. D. King, and G. L. Stephens (1996), Spectral reflectance and atmospheric energetics in cirrus-like clouds. Part II: Applications of a Fourier-Riccati approach to radiative transfer, *J. Atmos. Sci.*, *53*, 3450–3467.

Warren, S. G. (1984), Optical constants of ice from the ultraviolet to the microwave, *Appl. Opt.*, *23*, 1206–1225.

Wendisch, M., P. Pilewskie, E. Jäkel, S. Schmidt, J. Pommier, S. Howard, H. H. Jonsson, H. Guan, M. Schröder, and B. Mayer (2004), Airborne measurements of areal spectral surface albedo over different sea and land surfaces, *J. Geophys. Res.*, *109*, D08203, doi:10.1029/2003JD004392.

Yang, P., and K. N. Liou (1996), Geometric-optics-integral-equation method for light scattering by nonspherical ice crystals, *Appl. Opt.*, *35*, 6568–6584.

Yang, P., K. N. Liou, K. Wyser, and D. Mitchell (2000), Parameterization of the scattering and absorption properties of individual ice crystals, *J. Geophys. Res.*, *105*, 4699–4718.

Yang, P., M. G. Mlynczak, H. L. Wei, D. P. Kratz, B. A. Baum, Y. X. Hu, W. J. Wiscombe, A. Heidinger, and M. I. Mishchenko (2003), Spectral signature of cirrus clouds in the far-infrared region: Single-scattering calculation and radiative sensitivity study, *J. Geophys. Res.*, *108*(D18), 4569, doi:10.1029/2002JD003291.

Zhang, Y., A. Macke, and F. Albers (1999), Effect of crystal size spectrum and crystal shape on stratiform cirrus radiative forcing, *Atmos. Res.*, *52*, 59–75.

D. Baumgardner, Centro de Ciencias de la Atmósfera – UNAM, Universidad Nacional Autónoma de México, Circuito Exterior s/n, Ciudad Universitaria, 04510 México City (D.F.), México. (darrel@servidor.unam.mx)

A. J. Heymsfield and C. G. Schmitt, National Center for Atmospheric Research (NCAR), 3450 Mitchell Lane, Boulder, CO 80301, USA. (heyms1@ucar.edu; schmittc@ucar.edu)

S. Howard and J. Pommier, Bay Area Environmental Research (BAER) Institute, 560 Third Street West, Sonoma, CA 95476, USA. (howard@solat.arc.nasa.gov; jpommier@mail.arc.nasa.gov)

B. Mayer, Institut für Physik der Atmosphäre, Deutsches Zentrum für Luft- und Raumfahrt (DLR), Oberpfaffenhofen, D-82234 Wessling, Germany. (bernhard.mayer@dlr.de)

P. Pilewskie, Laboratory for Atmospheric and Space Physics (LASP), Program in Atmospheric and Oceanic Science, University of Colorado, Boulder, CO 80309, USA. (peter.pilewskie@lasp.colorado.edu)

M. Wendisch, Leibniz-Institut für Troposphärenforschung (IfT), Permoserstraße. 15, D-04318 Leipzig, Germany. (wendisch@tropos.de)

P. Yang, Department of Atmospheric Sciences, Texas A&M University, TAMU 3150, College Station, TX 77843, USA. (pyang@ariel.met.tamu.edu)